Sustainable Energy & Fuels

PAPER

View Article Online
View Journal | View Issue



Cite this: *Sustainable Energy Fuels*, 2018, 2, 2502

# MOFs as an electron-transfer-bridge between a dye photosensitizer and a low cost $Ni_2P$ co-catalyst for increased photocatalytic $H_2$ generation†

Li Wu,‡[a] Youchi Tong,‡[a] Lina Gu,[a] Zhaoming Xue[a] and Yupeng Yuan *[ab]

Received 9th April 2018
Accepted 14th May 2018

DOI: 10.1039/c8se00168e

rsc.li/sustainable-energy

Weak interaction results in inefficient electron transfer from the photoexcited erythrosin B dye photosensitizer to $H_2$ generation co-catalyst $Ni_2P$, thereby leading to low $H_2$ generation. To address this issue, UiO-66 MOFs were used as a suitable medium for enhancing the electron transfer process. The strong π–π interaction between the benzene rings of erythrosin B dye and UiO-66 ensures efficient electron transfer from the photoexcited erythrosin B dye to UiO-66. In addition, UiO-66 can serve as the substrate for growing the $Ni_2P$ co-catalyst. As a result, the erythrosin B dye/UiO-66/$Ni_2P$ system offers efficient electron transfer from erythrosin B dye to UiO-66, and to $Ni_2P$, thereby resulting in an active $H_2$ generation when compared to the erythrosin B dye and $Ni_2P$ system. The erythrosin B dye/UiO-66/$Ni_2P$ system with an optimum $Ni_2P$ amount of 0.69 wt% exhibits the highest $H_2$ evolution rate of 65 μmol $h^{-1}$. This value is nearly 5 times higher than that of the reference system without UiO-66 (13.8 μmol $h^{-1}$). The present results show the great potential of MOFs as a porous medium for enhancing the photocatalytic $H_2$ generation performance of conventional systems containing a photosensitizer and $H_2$ generation co-catalyst.



## Introduction

Photocatalytic $H_2$ generation is one of the most promising solutions to problems of energy shortage and environmental pollution.[1–7] The systems developed for photocatalytic $H_2$ generation always contain three parts: a photosensitizer for light absorption, a noble-metal-based co-catalyst for catalyzing $H_2$ generation, and a sacrificial electron donor for capturing holes photogenerated by the photosensitizer.[8,9] Presently, molecular dyes and noble metals are widely used to construct photocatalytic systems for $H_2$ generation despite the low efficiency. The low $H_2$ generation results from the insufficient charge transfer from photoexcited dyes to noble metals due to their weak interactions. To address this issue, an inorganic catalyst, such as $TiO_2$, was used as a medium to strengthen the interaction between dyes and noble metals as $TiO_2$ can serve as the substrate for dye absorption and co-catalyst loading.[10–16] However, the low absorption capacity of $TiO_2$ and weak interaction between $TiO_2$ and dyes show a less than anticipated enhancement in $H_2$ generation.[17,18]

MOFs are one of the most suitable media for bridging photosensitizers and $H_2$ generation co-catalysts.[19,20] MOFs are porous solids that are crystallized using metal ions and organic linkers. Compared to $TiO_2$, the advantages of using MOFs as a substrate for absorbing dyes and loading co-catalysts are twofold. First, MOFs have a large surface area and high pore volume, thus leading to a high absorption capacity for dyes. In addition, there exists strong π–π interaction between the benzene rings of MOFs and dyes, further improving the interaction between MOFs and dyes.[19,21] Consequently, the high adsorption capacity and strong π–π interaction ensure efficient charge transfer from photoexcited dyes to MOFs. Second, the functionalized organic linkers make MOFs a suitable substrate for growing inorganic co-catalysts. As a result, efficient charge transfer from photoexcited dyes to MOFs and then to co-catalysts for $H_2$ generation is expected in principle.

Herein we report a $H_2$ generation system containing erythrosin B dye, UiO-66 MOFs, and non-noble metal co-catalyst $Ni_2P$. This $H_2$ generation system has two advantages. First, MOFs were used as the "bridging medium" for enhancing the charge transfer from the photoexcited dye to the $H_2$ generation co-catalyst in spite of the fact that MOFs are photocatalysts for $H_2$ generation under UV/vis light irradiation.[22–26] Second, the co-catalyst is $Ni_2P$ rather than noble metals, such as Pt. Transition-metal phosphides (TMPs) have been a focus of research in electrochemical catalysis due to their noble-metal-free and

[a]*School of Chemistry and Chemical Engineering, Anhui Province Key Laboratory of Chemistry for Inorganic/Organic Hybrid Functionalized Materials, Anhui University, Hefei 230601, P. R. China. E-mail: yupengyuan@ahu.edu.cn*

[b]*Institute of Physical Science and Information Technology, Anhui University, Hefei 230601, P. R. China*

† Electronic supplementary information (ESI) available: SEM and TEM images; XRD patterns; $N_2$ adsorption–desorption isotherm; XPS spectra; and TG analysis. See DOI: 10.1039/c8se00168e

‡ Li Wu and Youchi Tong contributed equally to this work.

earth-abundant nature despite their relatively low electrocatalytic activity compared to noble metals.[27–30] The erythrosin B dye/UiO-66/$Ni_2P$ system shows a $H_2$ generation rate of 65 μmol $h^{-1}$, which is nearly 5 times higher than that of the reference system of erythrosin B dye/$Ni_2P$ (13.8 μmol $h^{-1}$).

Fig. 1a schematically shows the procedure for UiO-66/$Ni_2P$ preparation. UiO-66 octahedra were first prepared, and then $Ni(OH)_2$ was hydrothermally grown on the UiO-66 surface. Finally, $Ni(OH)_2$ was *in situ* converted to nickel phosphide ($Ni_2P$) nanoparticles by phosphating $Ni(OH)_2$/UiO-66 composites at 300 °C for 2 h in an Ar atmosphere. The obtained products were denoted as UiO-66/$Ni_2P$-*x* (*x* is the $Ni_2P$ weight ratio in the hybrids, and was determined to be $x = 0.35$, 0.69, 1.38, and 2.76 wt% from the amount of $Ni^{2+}$ added, assuming that $Ni^{2+}$ ions were totally converted to $Ni_2P$ and the amount of UiO-66 remained unchanged). Pristine UiO-66 is composed of octahedral microcrystals with an edge length of 200 to 500 nm (Fig. 1b). $Ni(OH)_2$ loading does not change the morphology of UiO-66 octahedra (Fig. 1c). The SEM image does not show the presence of $Ni(OH)_2$ particles on the surface of UiO-66 octahedra. However, the EDS result clearly confirms the presence of Ni as shown in Fig. S1.† In sharp contrast, several particles were observed on the surface of UiO-66 octahedra after phosphating the UiO-66/$Ni(OH)_2$ composites at 300 °C for 2 h in an Ar atmosphere (Fig. 1d). These small particles should be derived from $Ni(OH)_2$ as pristine UiO-66 octahedra retain their very smooth and clean surfaces after being thermally treated under the same conditions (Fig. S2†) as UiO-66 can be thermally stable up to 500 °C in Ar as shown in Fig. S3.†

The small $Ni_2P$ particles on UiO-66 octahedra were further examined by TEM analysis (Fig. 1e). These small particles are $Ni_2P$ as supported by high resolution TEM (HRTEM) analysis (Fig. 1f). HRTEM reveals a lattice fringe of 0.22 nm, indexed to the (111) planes of $Ni_2P$.[31] $Ni_2P$ nanoparticles about 20 nm in diameter were found to be intimately adhering to the surface of UiO-66 octahedra (Fig. 1e). A clear interface between UiO-66 and $Ni_2P$ was formed during phosphating $Ni(OH)_2$, which is very important for efficient charge transfer between UiO-66 and $Ni_2P$ and is thereby expected to improve the photocatalytic hydrogen production. EDS shows a molar ratio of 2.4 : 1 for $Ni_2P$ (Fig. 1g), which is very close to the theoretical ratio of 2 : 1. The uniform distribution of $Ni_2P$ on UiO-66 was further supported by elemental mapping (Fig. 1h).

The XRD patterns of UiO-66/$Ni_2P$ are shown in Fig. 2a. The XRD pattern of pristine UiO-66 has very sharp diffraction peaks, and all peaks can be indexed to UiO-66.[32] No peaks of byproducts were detected during the phosphating process for $Ni_2P$ formation. No peaks can be indexed to $Ni_2P$ likely owing to the low loading amount. The peaks at 30.5°, 40.8°, 44.6°, 47.3° and 54.4° are indexed to the (110), (111), (021), (210) and (002) facets, respectively. The XRD peaks are well matched with those of $Ni_2P$ (JCPDS#65-3544). FT-IR analysis (Fig. 2b) further supports the unchanged crystal structure of UiO-66 after $Ni_2P$ formation. XPS analysis was performed to further examine the characteristics of UiO-66/$Ni_2P$-0.69%. Fig. 2c and d show the Ni 2p and P 2p high-magnification XPS spectra, respectively. The two peaks at 853.8 and 856.8 eV for Ni $2p_{3/2}$ correspond to $Ni^{\delta+}$ and $Ni^{2+}$ of $Ni_2P$, respectively.[33,34] The peak at around 862.3 eV is the satellite of Ni $2p_{3/2}$.[35] Similarly, two peaks are observed at around 874.3 and 881.5 eV for the Ni $2p_{1/2}$ level, which are attributed to the $Ni^{2+}$ and satellite of $Ni_2P$, respectively.[33] In the P 2p XPS spectrum (Fig. 2d), the peak at 133.4 eV corresponds to P $2p_{1/2}$.[36] These results clearly indicate the presence of $Ni_2P$ in the obtained products.

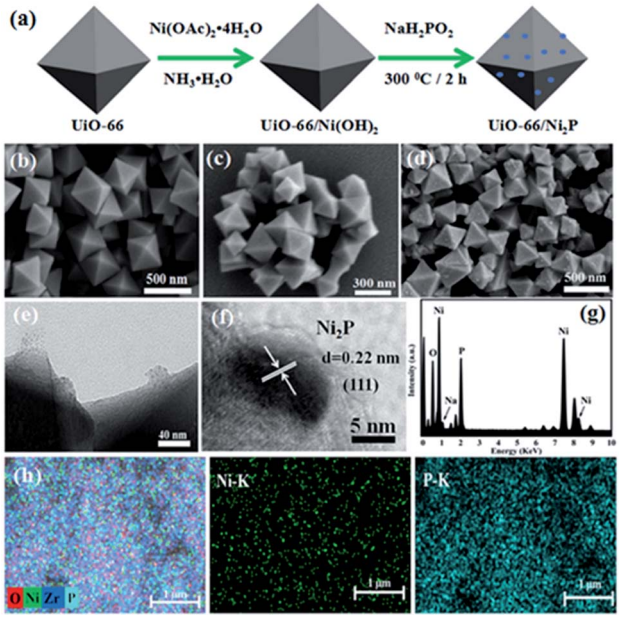


Fig. 1 (a) Schematic illustration of the $Ni_2P$/UiO-66 hybrids. SEM images of (b) pristine UiO-66, (c) UiO-66/$Ni(OH)_2$, and (d) UiO-66/$Ni_2P$-0.69%. TEM images of (e) UiO-66/$Ni_2P$-0.69% and (f) HRTEM images of $Ni_2P$ nanoparticles. (g) EDS spectrum of pure $Ni_2P$. (h) SEM-EDS elemental mapping of the UiO-66/$Ni_2P$-0.69% hybrid.

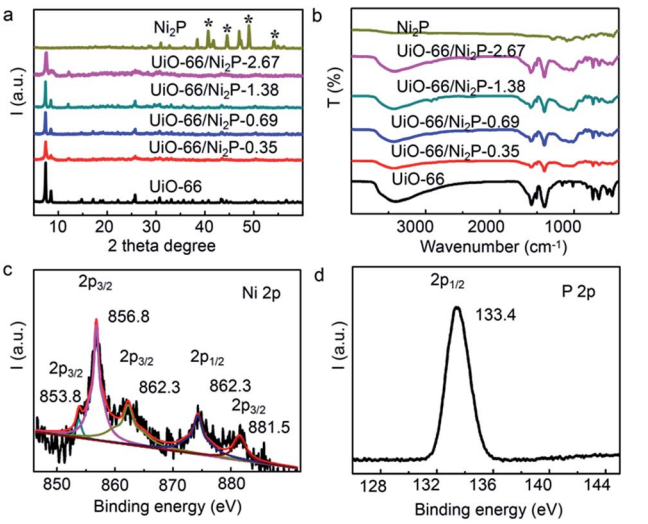


Fig. 2 (a) XRD patterns and (b) FT-IR spectra of the UiO-66/$Ni_2P$-*x* (*x* = 0.35, 0.69, 1.38, and 2.76 wt%) hybrids, pristine UiO-66 and $Ni_2P$. XPS spectra of (c) Ni 2p and (d) P 2p for UiO-66/$Ni_2P$-0.69%.

The UV/Vis absorption spectra of pristine UiO-66, $Ni_2P$, and the UiO-66/$Ni_2P$ composites are compared in Fig. 3a. Pristine UiO-66 exhibits an ultraviolet light absorption edge of 350 nm, corresponding to a 3.5 eV band gap.[20] The UiO-66/$Ni_2P$ composites also show the typical optical absorption behaviour of UiO-66 with an absorption edge of 350 nm. In addition, $Ni_2P$ loading results in intense light absorption in the visible light region. The more intense light absorption with increasing $Ni_2P$ loading supports the increased $Ni_2P$ content in UiO-66/$Ni_2P$ composites as exemplified by the $Ni_2P$ absorption spectrum.

Effective electron transfer depends largely on interactions among erythrosin B dye, UiO-66 MOFs, and the $Ni_2P$ co-catalyst. In this context, the steady-state photoluminescence (PL) upon excitation at 450 nm was measured in order to reveal the electron transfer among erythrosin B dye, UiO-66 MOFs, and $Ni_2P$ (Fig. 3b). Erythrosin B dye alone has a strong PL peak at 606 nm. In sharp contrast, UiO-66 addition significantly quenches this peak, verifying the efficient charge transfer from the photoexcited erythrosin B dye to UiO-66. Notably, the blue-shift of the PL peak from 606 nm to 601 nm further reveals the strong interaction between erythrosin B dye and UiO-66 MOFs. Moreover, $Ni_2P$ integration further decreases this PL peak, supporting the efficient electron transfer from erythrosin B dye to UiO-66, and then to $Ni_2P$.

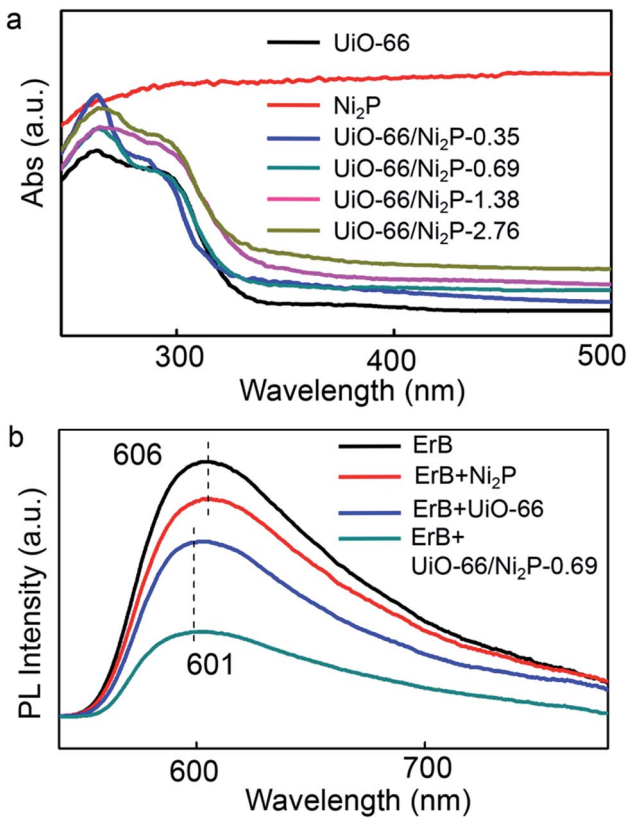


Fig. 3 (a) UV-vis diffuse reflectance spectra of pristine UiO-66, $Ni_2P$, and the UiO-66/$Ni_2P$-$x$ ($x$ = 0.35, 0.69, 1.38, and 2.76 wt%) hybrids. (b) Steady-state photoluminescence (PL) spectra of various systems: erythrosin B, erythrosin B and $Ni_2P$, erythrosin B and UiO-66, and the erythrosin B dye and UiO-66/$Ni_2P$-0.69 hybrid.

To uncover the effect of UiO-66 incorporation on $H_2$ generation, the erythrosin B/UiO-66/$Ni_2P$ system was tested for visible-light-response photocatalytic $H_2$ generation from water reduction. TEOA (10%) was used as the sacrificial electron donor. For utilizing visible light, erythrosin B dye was chosen to photosensitize UiO-66 owing to the strong interaction between their benzene rings, as revealed by the PL results shown in Fig. 3b. Control experiments show no $H_2$ generation without light irradiation or UiO-66/$Ni_2P$ catalysts. The $H_2$ generation rate was dependent on the concentration of erythrosin B. The highest $H_2$ generation rate of 65 μmol $h^{-1}$ was achieved when using 30 mg of erythrosin B dye for UiO-66/$Ni_2P$ (0.69 wt%) in 10 mL 10 vol% TEOA solution (Fig. 4a). All experiments were therefore tested under these conditions.

Fig. 4b shows the average $H_2$ generation rate in the first four hours. The system of erythrosin B dye and $Ni_2P$ offers a $H_2$ generation rate of 13.8 μmol $h^{-1}$ (Fig. 4c). In sharp contrast, the introduction of UiO-66 MOFs leads to a greatly increased $H_2$ generation rate (Fig. 4b and c). For example, the erythrosin B/UiO-66/$Ni_2P$-0.35 system shows a $H_2$ generation rate of 55.7 μmol $h^{-1}$ (Fig. 4b). This enhancement in $H_2$ generation is substantially benefited by the strong π–π interaction between the benzene rings of UiO-66 and erythrosin B dye, and thereby leads to efficient charge transfer from the photoexcited dye to UiO-66 MOFs. The very low $H_2$ generation from pure UiO-66 (~3.3 μmol $h^{-1}$) (Fig. 4b) further validates the essential role of MOFs in bridging the erythrosin B dye and $Ni_2P$ co-catalyst. Higher $Ni_2P$ coverage on UiO-66 leads to larger interfacial

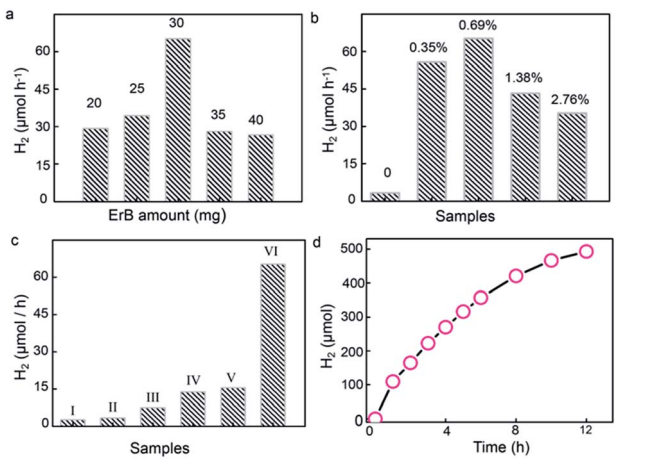


Fig. 4 (a) Effect of erythrosin B dye amount on the photocatalytic $H_2$ generation performance of the UiO-66/$Ni_2P$-0.69 hybrid. (b) Effect of $Ni_2P$ amount on photocatalytic $H_2$ generation; the number on the bars show the $Ni_2P$ content in the UiO-66/$Ni_2P$-$x$ hybrid. (c) Photocatalytic $H_2$ generation on various photocatalytic systems: (I) erythrosin B dye alone under visible light irradiation; (II) erythrosin B dye sensitized UiO-66 under visible light irradiation; (III) erythrosin B dye sensitized phosphatation-treated UiO-66; (IV) an erythrosin B dye suspension containing $Ni_2P$ (the amount is the same as that in the UiO-66/$Ni_2P$-0.69 hybrid); (V) a suspension of erythrosin B dye, pristine UiO-66, and $Ni_2P$ (the amount is the same as that in the UiO-66/$Ni_2P$-0.69 hybrid); and (VI) the erythrosin B dye sensitized UiO-66/$Ni_2P$-0.69 hybrid. (d) Long-term stability for photocatalytic $H_2$ generation on the UiO-66/$Ni_2P$-0.69 hybrid.

areas, more efficient charge separation and thereby the higher $H_2$ generation rate as exemplified by the $H_2$ generation rate of 65 μmol $h^{-1}$ observed for the erythrosin B/UiO-66/$Ni_2P$ (0.69 wt%) system. This value is nearly 5 times greater than that of the system without UiO-66 MOFs. It is also worth highlighting the necessity of the *in situ* formation of $Ni_2P$ for enhanced $H_2$ generation. A simple physical mixture of $Ni_2P$ (0.69 wt%) and UiO-66 shows a $H_2$ generation rate of 15.5 μmol $h^{-1}$ under the same experimental conditions (Fig. 4c). This result clearly exemplifies the importance of the *in situ* phosphating process which ensures the formation of tight $Ni_2P$/UiO-66 interfaces for efficient charge transfer from the photoexcited dye to UiO-66 and to $Ni_2P$. However, reduced $H_2$ generation performance is observed when the $Ni_2P$ content is further increased to 1.38 wt% (UiO-66/$Ni_2P$-1.38) and 2.76 wt% (UiO-66/$Ni_2P$-2.76) (Fig. 4b). This result is ascribed to the concomitant coverage effect in which the overloading of $Ni_2P$ can cause the active sites for $H_2$ evolution to be covered, and thereby hinder the $H_2$ generation as no obvious difference in size and morphology of $Ni_2P$ at low (0.35 wt%) and high (2.76 wt%) loading amounts can be observed (Fig. S4†). It is worth noting that there is Na species in the obtained $Ni_2P$/UiO-66 hybrids as shown by the EDS result (Fig. 1g). The Na signal in Fig. 1g should originate from $NaH_2PO_2$, which was added as the P source for phosphating UiO-66/$Ni(OH)_2$ to UiO-66/$Ni_2P$. To verify the effect of Na on photocatalytic activity, we tested the $H_2$ generation activity by adding $NaH_2PO_2$ (25 mg) into the reaction suspension while keeping other experimental factors unchanged. No evident change in $H_2$ generation was observed (Fig. S5†), validating that Na species in UiO-66/$Ni_2P$ hardly contribute to photocatalytic $H_2$ generation despite a slight change of pH value from 9.3 for the original suspension to 10 after $NaH_2PO_2$ addition. This result is ascribed to NaOH formation through the reaction of $NaH_2PO_2$ with triethanolamine, the sacrificial electron donor.

$Ni_2P$ as a non-noble-metal co-catalyst has excellent photostability for photocatalytic $H_2$ generation.[4,37] To test the stability of $Ni_2P$ in the present system, UiO-66/$Ni_2P$-0.69 was used as a representative sample for long term photocatalytic $H_2$ generation. Impressively, UiO-66/$Ni_2P$-0.69 shows a relatively stable $H_2$ generation profile over the duration of a 12 h reaction (Fig. 4d). The slight decrease in $H_2$ evolution is a common phenomenon in dye sensitized photocatalysts for $H_2$ generation as the dye would gradually be consumed and deactivated.[38,39] XRD analysis validates the unchanged phase of UiO-66/$Ni_2P$-0.69 before and after 12 h of $H_2$ generation reaction (Fig. S6†). In addition, neither aggregation nor any phase or morphology change for $Ni_2P$ was detected after 12 h of long-term $H_2$ generation reaction (Fig. S7†). This result further supports the fact that $Ni_2P$ stability plays an important role in boosting $H_2$ generation.

The increased $H_2$ generation is the result of the efficient electron transfer from the photoexcited erythrosin B dye to UiO-66 and then to the $Ni_2P$ co-catalyst, as revealed by stable-state PL analysis. It has been reported that the LUMO potential of erythrosin B dye (−0.9 V *vs.* NHE at pH 7.0)[40] is more negative than the conduction band edge of UiO-66 (−0.6 V *vs.* NHE at pH 7.0).[20] In addition, there are strong π–π stacking interactions and van der Waals forces between the benzene rings of erythrosin B dye and UiO-66 MOFs as exemplified by the blue-shift of the photoluminescence peak in Fig. 3b. Moreover, the large surface area of UiO-66 (Fig. S8†) further ensures the large absorption of the dye on MOFs. As consequence, the electrons in the photoexcited erythrosin B dye could thus effectively transfer to UiO-66 MOFs (Fig. S9†). The electrons injected into UiO-66 could further transfer to $Ni_2P$ across the UiO-66/$Ni_2P$ interfaces created by *in situ* phosphatation, and the electrons accumulating on $Ni_2P$ can reduce $H^+$ to hydrogen.

In order to verify the enhanced charge separation of erythrosin B/UiO-66/$Ni_2P$(0.69 wt%), photoelectrochemical (PEC) *I–T* curves, electrochemical impedance spectroscopy (EIS) plots, and polarization curves were further measured and are shown in Fig. 5. In Fig. 5a, the photocurrent responses were prompt and reproducible during the on/off cycles of visible-light excitation; the higher photocurrent of erythrosin B/UiO-66/$Ni_2P$-0.69 indicated the fast electron transfer from erythrosin B to UiO-66 to $Ni_2P$ and then to ITO glass. Fig. 5b presents the EIS Nyquist plots of erythrosin B/UiO-66 and erythrosin B/UiO-66/$Ni_2P$ (0.69 wt%). Since the arc radius of erythrosin B/UiO-66/$Ni_2P$ (0.69 wt%) is smaller than that of erythrosin B/UiO-66, it demonstrates that the loaded $Ni_2P$ co-catalyst can effectively

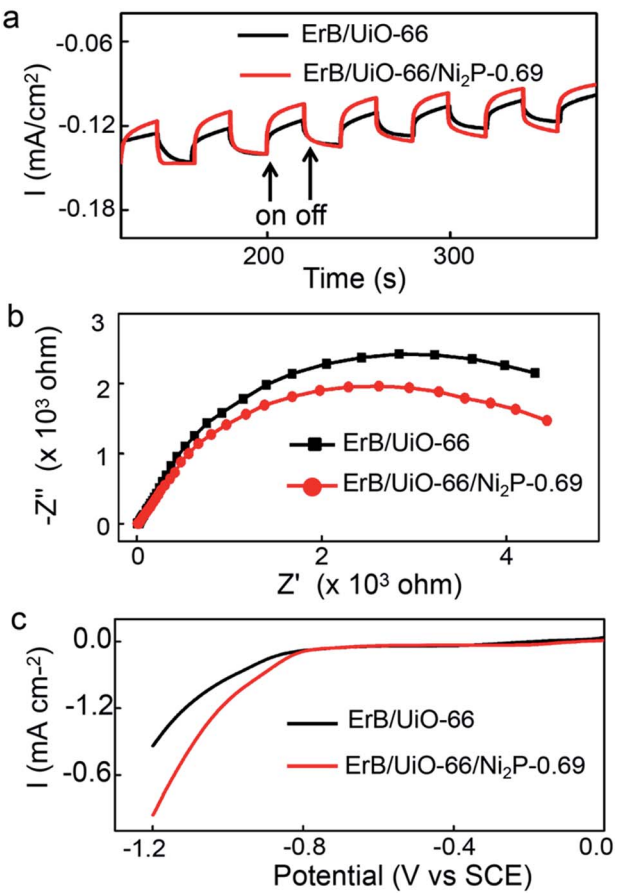


Fig. 5 (a) Comparison of transient photocurrent responses under visible-light irradiation, (b) EIS Nyquist plots, and (c) polarization curves of the ErB/UiO-66 and ErB/UiO-66/$Ni_2P$-0.69 hybrids.

promote the charge transfer at the photocatalyst/solution interface, corresponding to the result of the enhanced photocatalytic activity. Also from the polarization curves (Fig. 5c), erythrosin B/UiO-66/$Ni_2P$-0.69 exhibits much more pronounced cathodic current density and lower overpotential compared to ErB/UiO-66, which demonstrates that the erythrosin B/UiO-66/$Ni_2P$-0.69 interfaces can efficiently enhance the electron mobility by reducing the recombination of photogenerated carriers, thus presenting the increased hydrogen generation rate.

In summary, UiO-66 MOFs were exemplified as an excellent electron transfer channel for bridging the erythrosin B dye and $Ni_2P$ co-catalyst. The high adsorption capacity, suitable band energy position, and strong π–π interaction with the dye make UiO-66 MOFs a suitable medium for accepting electrons from the photoexcited erythrosin B dye. Moreover, the intimate adhering of $Ni_2P$ on UiO-66 octahedra guarantees electron transfer across the interfaces of UiO-66 and $Ni_2P$ to $Ni_2P$ nanoparticles. This efficient charge transfer process suppresses the recombination of electron–hole pairs, leading to enhanced $H_2$ generation. The present work shows the great potential of MOFs for photocatalytic $H_2$ generation.

## Conflicts of interest

There are no conflicts to declare.

## Acknowledgements

This work was financially supported by the National Natural Science Foundation of China (51572003) and Anhui Provincial Natural Science Foundation (1508085ME105). Dr Yuan acknowledges the financial support of SRF for ROCS, SEM, and the Technology Foundation for Selected Overseas Chinese Scholars.

## Notes and references

1 K. Maeda, K. Teramura, D. Lu, T. Takata, N. Saito, Y. Inoue and K. Domen, *Nature*, 2006, **440**, 295.
2 Y. P. Yuan, L. W. Ruan, J. Barber, S. C. J. Loo and C. Xue, *Energy Environ. Sci.*, 2014, **7**, 3934–3951.
3 J. Ran, J. Zhang, J. Yu, M. Jaroniec and S. Z. Qiao, *Chem. Soc. Rev.*, 2014, **43**, 7787–7812.
4 Z. Sun, H. Zheng, J. Li and P. Du, *Energy Environ. Sci.*, 2015, **8**, 2668–2676.
5 X. Li, J. Yu and M. Jaroniec, *Chem. Soc. Rev.*, 2016, **45**, 2603–2636.
6 R. B. Wei, Z. L. Huang, G. H. Gu, Z. Wang, L. Zeng, Y. Chen and Z. Q. Liu, *Appl. Catal., B*, 2018, **231**, 101–107.
7 C. Huang, T. Ouyang, Y. Zou, N. Li and Z. Q. Liu, *J. Mater. Chem. A*, 2018, **6**, 7420–7427.
8 X. Chen, S. Shen, L. Guo and S. S. Mao, *Chem. Rev.*, 2010, **110**, 6503–6570.
9 A. Kudo and Y. Miseki, *Chem. Soc. Rev.*, 2009, **38**, 253–278.
10 Y. Li, M. Guo, S. Peng, G. Lu and S. Li, *Int. J. Hydrogen Energy*, 2009, **34**, 5629–5636.
11 X. Liu, Y. Li, S. Peng, G. Lu and S. Li, *Photochem. Photobiol. Sci.*, 2013, **12**, 1903–1910.
12 Y. Li, C. Xie, S. Peng, G. Lu and S. Li, *J. Mol. Catal. A: Chem.*, 2008, **282**, 117–123.
13 M. Ye, M. Wang, D. Zheng, N. Zhang, C. Lin and Z. Lin, *Nanoscale*, 2014, **6**, 3576–3584.
14 M. Wang, D. Zheng, M. Ye, C. Zhang, B. Xu, C. Lin, L. Sun and Z. Lin, *Small*, 2015, **11**, 1436–1442.
15 M. Wang, L. Sun, Z. Lin, J. Cai, K. Xie and C. Lin, *Energy Environ. Sci.*, 2013, **6**, 1211–1220.
16 M. Wang, X. Pang, D. Zheng, Y. He, L. Sun, C. Lin and Z. Lin, *J. Mater. Chem. A*, 2016, **4**, 7190–7199.
17 R. Abe, K. Hara, K. Sayama, K. Domen and H. Arakawa, *J. Photochem. Photobiol., A*, 2000, **137**, 63–69.
18 R. Abe, K. Sayama and H. Arakawa, *J. Photochem. Photobiol., A*, 2004, **166**, 115–122.
19 X. L. Liu, R. Wang, M. Y. Zhang, Y. P. Yuan and C. Xue, *APL Mater.*, 2015, **3**, 37.
20 Y. P. Yuan, L. S. Yin, S. W. Cao, G. S. Xu, C. H. Li and C. Xue, *Appl. Catal., B*, 2015, **168–169**, 572–576.
21 J. He, J. Wang, Y. Chen, J. Zhang, D. Duan, Y. Wang and Z. Yan, *Chem. Commun.*, 2014, **50**, 7063.
22 L. Jiao, Y. Wang, H. L. Jiang and Q. Xu, *Adv. Mater.*, 2017, 1703663.
23 Z. Li, J. Xiao and H. Jiang, *ACS Catal.*, 2016, **6**, 5359–5365.
24 X. Fang, Q. Shang, Y. Wang, L. Jiao, T. Yao, Y. Li, Q. Zhang, Y. Luo and H. L. Jiang, *Adv. Mater.*, 2018, 1705112.
25 J. D. Xiao and H. L. Jiang, *Small*, 2017, **13**, 1700632.
26 J. D. Xiao, Q. Shang, Y. Xiong, Q. Zhang, Y. Luo, S. H. Yu and H. L. Jiang, *Angew. Chem.*, 2016, **128**, 9535–9539.
27 P. Liu and J. A. Rodriguez, *J. Am. Chem. Soc.*, 2005, **127**, 14871–14878.
28 X. Zhu, M. Liu, Y. Liu, R. Chen, Z. Nie, J. Li and S. Yao, *J. Mater. Chem. A*, 2016, **4**, 8974–8977.
29 Y. Pan, N. Yang, Y. Chen, Y. Lin, Y. Li, Y. Liu and C. Liu, *J. Power Sources*, 2015, **297**, 45–52.
30 L. Yan, P. Dai, W. Ying, G. Xin, L. Li, C. Lei and X. Zhao, *ACS Appl. Mater. Interfaces*, 2017, **9**, 11642.
31 R. K. Chiang and R. T. Chiang, *Inorg. Chem.*, 2007, **46**, 369–371.
32 M. Kandiah, M. H. Nilsen, S. Usseglio, S. Jakobsen, U. Olsbye, M. Tilset, C. Larabi, E. A. Quadrelli, F. Bonino and K. P. Lillerud, *Chem. Mater.*, 2010, **22**, 6632–6640.
33 Y. Zhao, Y. Zhao, H. Feng and J. Shen, *J. Mater. Chem.*, 2011, **21**, 8137–8145.
34 D. P. Kumar, J. Choi, S. Hong, D. A. Reddy, S. Lee and T. K. Kim, 2016, **4**, 7158–7166.
35 A. N. Mansour, *Surf. Sci. Spectra*, 1994, **3**, 239–246.
36 A. P. Grosvenor, S. D. Wik, R. G. Cavell and A. Mar, *Inorg. Chem.*, 2006, **37**, 8988–8998.
37 G. F. Chen, T. Y. Ma, Z. Q. Liu, N. Li, Y. Z. Su, K. Davey and S. Z. Qiao, *Adv. Funct. Mater.*, 2016, **26**, 3314–3323.
38 W. Zhang, J. Hong, J. Zheng, Z. Huang, J. Zhou and R. Xu, *J. Am. Chem. Soc.*, 2011, **133**, 20680.
39 W. Zhang and R. Xu, *Int. J. Hydrogen Energy*, 2012, **37**, 17899–17909.
40 Y. Wang, J. Hong, W. Zhang and R. Xu, *Catal. Sci. Technol.*, 2013, **3**, 1703–1711.

 